



Origami-Inspired Wearable Robot for Trunk Support

Dongting Li[®], Graduate Student Member, IEEE, Emiliano Quinones Yumbla[®], Graduate Student Member, IEEE, Alyssa Olivas, Thomas Sugar[®], Senior Member, IEEE, Heni Ben Amor, Hyunglae Lee[®], Member, IEEE, Wenlong Zhang[®], Member, IEEE, and Daniel M. Aukes[®], Member, IEEE

Abstract—We present a wearable "exo-shell" device inspired by the human spine for improving the gait of elderly people during obstacle avoidance tasks. This device—designed and fabricated with origami-inspired techniques—features a serial chain of lockable joints that can be stiffened using a braking system inspired by laminar jamming concepts. Current related work has identified that the trunk plays a crucial role in obstacle avoidance tasks. In this article, we thus propose an affordable wearable system that can be quickly fabricated and whose design can be adjusted to fit the individual wearer. The design leverages switchable, passive systems, in combination with lightweight materials that remain as "transparent" to the user as possible when inactive. This article focuses on translating human requirements into a tangible design that addresses the current state of our biomechanics knowledge. We describe the kinematics and forces of our proposed device, describe the performance of our system in a locked and unlocked state, discuss the integration of various sensors into our device, and characterize the performance of the device when locked and unlocked.

Index Terms—Parallel robots, robotics and automation, robot kinematics, wearable robots.

I. Introduction

N THIS article, we propose a new class of wearable robotic devices called "exo-shells"—origami-inspired, multilink

Manuscript received 2 September 2022; accepted 27 October 2022. Date of publication 15 November 2022; date of current version 16 June 2023. Recommended by Technical Editor Zhuming Bi and Senior Editor W. J. Chris Zhang. This work was supported by a grant from "The Global KAITEKI Center" (TGKC) of the Global Futures Laboratory at Arizona State University. (Corresponding author: Daniel M. Aukes.)

Dongting Li, Thomas Sugar, Wenlong Zhang, and Daniel M. Aukes are with the School of Manufacturing Systems and Networks, Ira A. Fulton Schools of Engineering, Arizona State University, Mesa, AZ 85212 USA (e-mail: dongting@asu.edu; thomas.sugar@asu.edu; wenlong.zhang@asu.edu; danaukes@asu.edu).

Emiliano Quinones Yumbla, Alyssa Olivas, and Hyunglae Lee are with the School for Engineering of Matter, Transport and Energy, Ira A. Fulton Schools of Engineering, Arizona State University, Tempe, AZ 85212 USA (e-mail: ejquino1@asu.edu; alyssa.olivas@asu.edu; hyunglae.lee@asu.edu).

Heni Ben Amor is with the School of Computing and Augmented Intelligence, Ira A. Fulton Schools of Engineering, Arizona State University, Tempe, AZ 85212 USA (e-mail: hani.benamor@asu.edu).

This article has supplementary material provided by the authors and color versions of one or more figures available at https://doi.org/10.1109/TMECH.2022.3220136.

Digital Object Identifier 10.1109/TMECH.2022.3220136

robots with the ability to sense their state and stiffen selected regions on demand to guide, support, and nudge the wearer during daily living activities. Starting with a trunk support robot as a case study, the goal of our current system is to provide supportive forces for maintaining proper posture when avoiding obstacles during walking, with the intent to reduce the chance of slips, trips, and falls. The purpose of this article, therefore, is to outline the design and strategy for stiffening, sensing, and understanding its current performance across a wide range of physical considerations. The key contributions of this article may be summarized as follows:

- 1) we introduce an origami-inspired design approach to rapidly manufacture and customize wearable robots;
- 2) we implement this methodology to create a new serial robot with low resistance and switchable stiffness; and
- we introduce and validate the kinematic models for understanding the dimensional requirements for stiffening the robot against external loads using brakes.

The rest of the article is organized as follows: In Section II, we conduct a literature review surveying the state of the art in various wearable robotic technologies. We then introduce our design rationale and describe our approach in the design of each subsystem, along with the kinematic model of the device in Section III. Section IV then describes the experimental validation of our subsystems, kinematics, and system. This article concludes in Section V with some insights on the future of this research along with our thoughts on the impact of this design.

II. LITERATURE REVIEW

A variety of rigid exoskeletons have been developed for improving mobility over the decades [1], [2], [3], [4], [5], [6]. High forces and torques provided by those rigid exoskeletons assist the ankle, hip and/or knee, facilitating activities such as walking or lifting heavy objects. However, due to the complexity of the human musculoskeletal system, adjusting and aligning human and robot joints has proven difficult, increasing the metabolic cost of the wearer and the external energy expenditure of the attached system. Heavy, high-torque, and often nonbackdriveable systems can also be a safety risk for the wearer when the control system fails or misalignments occur [7], [8].

More recent innovations in soft robotic techniques [9], [10], [11], [12] have resulted in "exo-suit" style technology in which tendons routed through Bowden cables provide pulling forces

1083-4435 © 2022 IEEE. Personal use is permitted, but republication/redistribution requires IEEE permission. See https://www.ieee.org/publications/rights/index.html for more information.

across joints. While this has addressed many of the issues stemming from traditional exoskeleton designs, it has also resulted in increased forces across human joints, which can lead, over time, to damaging the user's joints through increased wear [13]. Furthermore, wearable robotic orthoses often fail to break even on metabolic cost, although there have been some notable recent exceptions [9], [14], [15]. One common nuance of a number of exoskeletons/suits is that they are often designed and tuned for one purpose, such as lifting, walking, running, or carrying loads. Fewer wearable devices provide the versatility required to be worn as a multipurpose device throughout the day, again with notable exceptions [16], [17], [18].

Many of the above wearable robotic systems employ active sensing and feedback control techniques to quickly respond to the wearer's motion and provide powered assistance both to assist the user as well as to offset the extra weight of the system itself. In many cases, however, the small control delays imposed by digital control techniques also add small but perceptible loads to the wearer that can over time lead to accelerated fatigue and reduced efficacy [19].

Thus, a middle ground between soft and rigid solutions is still desired, in which wearable systems provide alternate loading pathways across joints, where a variety of capabilities can be enabled or disabled on-demand based on the user's activity, and in which the tradeoff between wearability and utility is made not through the use of active, timed, energy addition via powered joints, but by minimizing the weight of rigid systems, and by powering the system to change its state.

Loaded mass or load carriage-induced metabolic costs have been well studied in elderly people during walking [20], [21], [22]. To create such "transparency" while preventing motion when engaged, one design approach is to reduce the overall weight of the device. Utilizing structural element only in a compliant mechanism [23] can be alternative method to meet this weight requirement. We then adapt concepts from soft robotics [24] and choose origami-inspired, laminate fabrication techniques as the fundamental technology for creating lightweight, high stiffness, and rapidly manufacturable wearable mechanisms. Having been applied to a variety of robotic applications [25], [26], [27], origami robots have also been shown to be capable of providing high structural stiffness [28], [29]. Furthermore, the incorporation of sensors into origami structures has proven itself to be a promising method for sensorizing modular origami segments [30], [31].

A variety of methods may be used to stiffen or lock origami mechanisms, including shape memory polymers (SMP) [32], bistable patterns [33], [34], [35], electrostatic jamming [36], and laminar jamming [37], [38]. Layer jamming in particular has proven itself compact and light weight while providing high locking forces [39], [40], [41], [42], [43], [44]. This technique typically employs a negative pressure gradient over soft membranes, either within a bag or distributed across a planar surface, to bring layered sliding materials into close contact. As the pressure grows, the friction between layers increases to slow and stop relative motion between layers. Pneumatic-based jamming, however, necessitates high-pressure negative differential pressures, which must be supplied by a vacuum pump. This is less ideal for compact, portable designs that must be worn,

TABLE I
COMPARISON OF TRUNK SUPPORT ROBOT FEATURES

Robot	Soft/ Rigid	Weight	Actuation Method	Passive/ Active
Yang et al [47]	Soft	Not reported	Bowden tubes	Passive
Lee et al [48]	Soft	1.3kg (without battery)	Twisted string actuator	Passive
Heo et al [49]	Rigid	9.2kg	Pneumatic	Active
Park et al [50]	Rigid	Not reported	Linear actuator	Active
This article	Soft	1.4 kg	Locking	Passive

because the size and weight of these pumps can be exceedingly large in order to achieve the required pressures through narrow tubing in a short amount of time. Mechanical clamping [41], [45], [46] can address some of those issues, permitting small, nonbackdriveable motors to generate high normal forces; we have thus selected this approach in our current prototype.

III. MATERIALS AND METHODS

A. Design Rationale

Requirement: Based on preliminary human motion data [51], we have determined that interventions along the sagittal plane at the wearer's trunk (waist) pose the best opportunity for reducing reaction torques in elderly users by providing external stiffness along the trunk. A detailed description of the experiments and validation can be seen in the Supplemental Material, Section SM-1 with features of existing trunk support robots [47], [48], [49], [50] compared and summarized in Table I. While less considering the metabolic cost induced by the weight of the robot, providing stiffness or locking force on demand and minimize frictions when unlocked are common features. To increase the mobility, these designs tend to create lightweight structures or propose integrating powering unit as future works. We then identify the requirements for a trunk support robot as the following:

- 1) lightweight;
- 2) low power consumption except when changing states; and
- 3) transparency when disengaged.

Past literature has established that metabolic cost increases with increased load [20], [21], and that the user will have more difficulty maintaining their center of mass. However, under certain load carriage cases, increased metabolic cost does not increase fatigue or reduce performance significantly. According to Grabowski et al. [22], for elderly human subjects (70 kg), payloads less than 3% (2.1 kg) of the human body do not significantly impact the wearer [52], [53]. Therefore, one design criterion is to keep our system weight below this value. Additionally the distribution of the load at the posterior of the trunk helps minimize metabolic cost by keeping system loads closer to the user's center of mass [21].

For the purposes of our design, our envisioned device is thus attached around the waist and just below the shoulder blades (as seen in Fig. 1) and stiffens on demand along the sagittal plane. To create the effect of a continuum system using origami-inspired approaches, we highlight four essential subcomponents of our design.

Components: The following subcomponents are required for our system:

1) rotational elements;

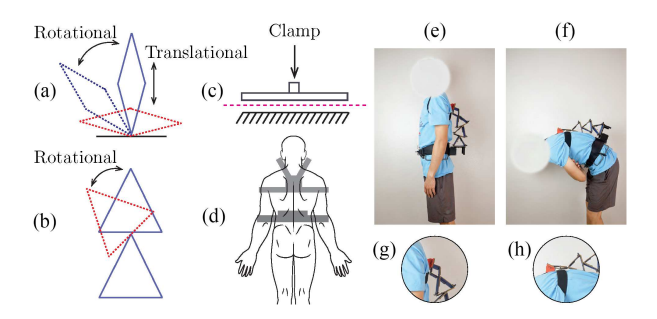


Fig. 1. Components of the robot. From (a) to (d), we show the four-bar linkage, triangle element, brake and mounting belts, respectively. Subfigures (e) and (f) illustrate the configuration change as a function of posture, where (e) stands for standing straight and (f) shows bending the trunk. We highlight the extraction of the four-bar linkage in (g) and (h). Upon bending, the distal four-bar linkage extends to maximum length to accommodate the human. In this set of figures, we show the robot without break to highlight the structural elements.

- 2) translational elements;
- 3) a locking mechanism; and
- 4) mounting components.

Because the base of the robot is mounted at the wearer's waist and beneath the shoulder blades, our system will need to both rotate and lengthen in order to conform to and support the wearer's back during trunk flexion.

Thus, both *rotational* and *translational* degrees of freedom (DOF) are required to fully adapt to the wearer's motion. We propose two basic elements as the building blocks for our device.

We use a laminate fabrication method to construct triangular links that serve as the serial "rotational" elements. Triangles have been selected for these one-DOF rotational elements because, as fundamental elements of trusses, they form stiff, light weight structures. The outer faces of the triangles serve as simple joint limits to restrict motion to a specific range, as well as the attachment point for our locking system; the range of motion may be adjusted by modifying the triangle's dimensions and proximal connection point. This adjustability serves as a useful way to adapt to individual users while achieving high stiffness using thin materials.

We have also selected a locking four-bar linkage as a secondary, more-complex component because it is capable of both rotation and translation in two degrees of freedom. This component is essential, as mentioned before, for permitting the serial chain to lengthen along the back during flexion. Fig. 5(a). highlights the motion and locking configurations under different external loading conditions.

A number of possible locking solutions have been reviewed for our system; we have selected a mechanical-based jamming brake to lock the system on demand. Brakes, in contrast with actuated joints, are light weight, respond quickly, and are compatible with tendons attached to multiple moving parts to permit global locking. Mounting components can be selected from a variety of commercially available hip harnesses, shoulder straps for the upper body, or other custom solutions.

B. Manufacturing and Device Customization

Following a laminate fabrication approach, as described in [54], [55], and [56], the mechanism is designed using 3-D computer-aided design (CAD) software. Each layer of the

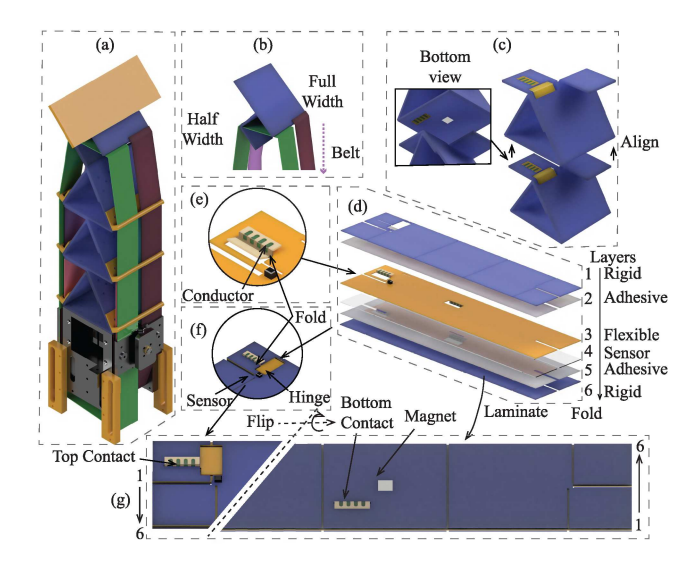


Fig. 2. Manufacturing of the origami-inspired system. (a) Assembled device. (b) Four-bar segment. (c) Aligned triangle segment with contact pads aligned to the previous segment. (d) Different material layers are stacked and aligned prior to lamination. The layer number and name can be seen on the rigid side. (e) and (f) A closer view of the conductors and sensors, showing how the contact pad is folded twice to expose the copper side to the next segment. (g) Top and bottom views of the laminated triangle segment, divided by the dashed line and flipped to see the bottom.

laminate is generated, exported, and cut with a laser using a custom Python script. The layers of the element are illustrated in Fig. 2(g). They consist of a sandwich of two, thick, rigid outer layers of material, followed by inner layers of adhesive, a flexible middle layer that serves as a living hinge, and a flexible circuit layer for mounting and connecting embedded sensors to power and communication. The rigid, adhesive, and hinge layers are cut with an Epilog Fusion M2 75 W CO₂ laser cutter; the flex-circuit layer is manufactured using a masking and chemical etching process. Four copper traces on the flex circuit layer permit communication using the I²C protocol to each sensor. All the layers are then aligned using locating pins and bonded using a heat press. After the circuit layer is laminated to the other layers, the full laminate is then cut away from remaining scrap with a final release cut.

After the segments are folded into their final configuration they are serially connected to the next element, as shown in Fig. 2(e). Once the positions of the circuit layer components are confirmed, the I²C bus can then be connected. The conductors from a proximal segment are aligned and connected to the next distal segment so that sensors integrated directly onto the flex circuit can communicate back to the microcontroller located in the base. More details on sensing, integration, and evaluation can be found in Sections SM-2 and SM-3.

For this version of the trunk support device, we have selected three triangle elements and one four-bar linkage in the construction of our serial chain, as shown in Fig. 2(a). Details on

¹[Online]. Available: https://github.com/iicfcii/laminate-pipeline

²Crescent Select Alpha-Cellulose Matboard

³Grafix Dura-Lar 5 mil

⁴DuPont Pyralux AP Copper-Clad Laminate ap7163e

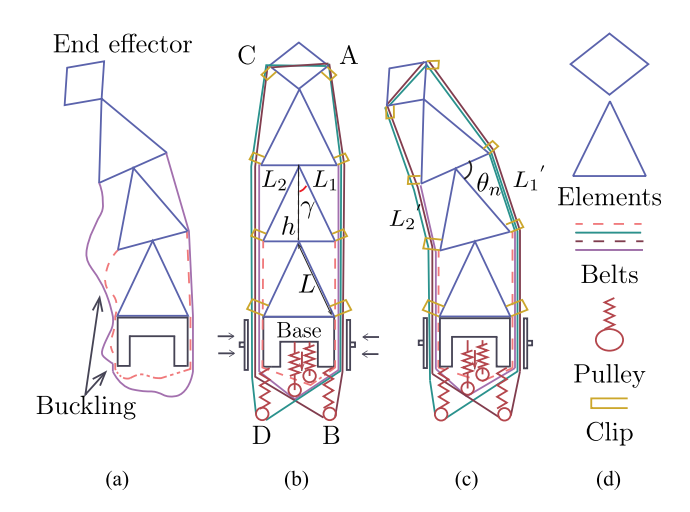


Fig. 3. Design and integration of the brake. In (a), we demonstrate how buckling might happen. (b) is a 2-D sketch of the spine where the tension mechanism and clips are integrated to the base station to prevent buckling. We label the different components with various color and line types. In (c), we show how the required length for the layers changes as a function of configuration. Legend (d) represents the components and accessories of this system.

dimensioning can be found in Section IV-B. Successive triangles are connected as shown in Fig. 2(a) and (e); the proximal joint of each link is located at a point along the triangle's base. The distal joint of each link is located at the top vertex of the triangle; the next most distal triangle's origin (also located along its base) is thus connected to this point. The four-bar linkage is then connected to the top vertex of the most distal triangular link to compensate for any lengthening during trunk flexion. The selected laminate manufacturing technique allows for rapid and low-cost customization for users with different trunk lengths; a detailed cost analysis as well as manufacturing breakdown is highlighted in Section SM-5.

C. Brake Design

The mechanical design of the brake consists of three main parts:

- flexible, sliding sheet-based belts attached to each moving segment of the wearable system,
- 2) a motorized clamp for applying normal forces to the belts, and
- 3) a tension mechanism that maintains tension in each belt to minimize backlash, as seen in Fig. 3(b).

In the triangular segments, one belt is attached to each side of the two lower vertices of the triangular segment, as shown in Fig. 3(b). The lower portion of these belts is clamped to the base of the device via two motorized, self-aligning brake pads in the base station. These clamps are actuated via lead screws to stepper motors, which are controlled by an Arduino UNO using a TB6600 stepper motor driver. When activated, the motors drive the lead screws to clamp the belts on each side of the base station, locking all the degrees of freedom together.

The length of the belt traveling around the base station and attaching to each segment is a function of system configuration, as seen in Fig. 3(c). For example, the total length of the layers

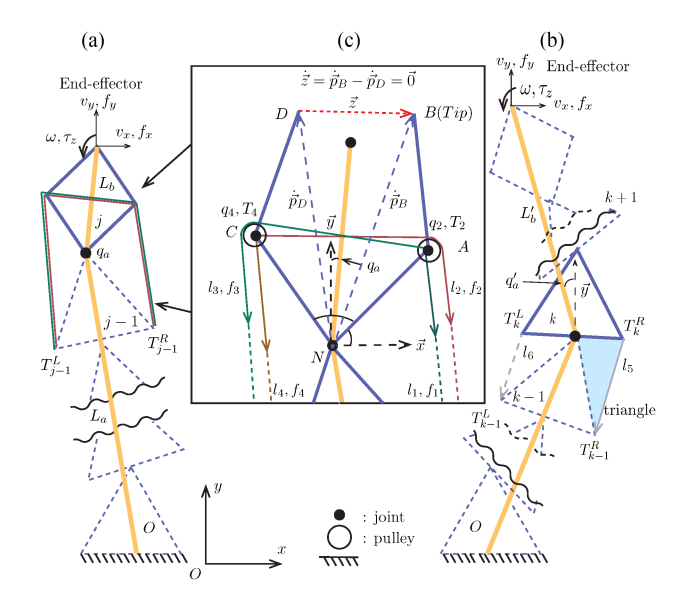


Fig. 4. Kinematic model. In (a), we show the simplified kinematic model of the *j*th four-bar element mounted on *j-1*th triangle, we also illustrate how belts are routed on the four-bar element and kinematics constraints in (c). Although the four-bar is a closed chain mechanism, we show these two RR chains split into chains NCD and NAB, constrained by \dot{z} (red line). We show how an example of how we relate a triangle at random location to the end-effector as shown in (b). Although we only have three triangles in our current design, we demonstrate how our method can be applied to one at a random location and orientation.

on the side $L_1 + L_2$ varies as $\sqrt{W^2/4 + L^2 - WL\cos(\theta_n)} + \sqrt{W^2/4 + L^2 - WL\cos(\pi - \gamma - \theta_n)}$ with a decrease of about 3.39% in length at its limit compared to $\theta_n = 0^\circ$. Excess slack in those configurations causes backlash in the system, which can lead to unintended shocks, misalignments, and unintended stresses in the belt, and can ultimately lead to premature damage of the system, as shown in Fig. 3(a). To prevent buckling and keep the layers flat within the clamping area, we have added 1) a tension mechanism that utilizes a spring-loaded pulley to maintain tension at the bottom of the belt and 2) 3-D printed clips with clearance to allow layers to slide while maintaining a position constraint at each segment's vertices, as shown in Fig. 3(b).

Two belts are attached in a similar way to the two-DOF four-bar segment at each end, in order to fully lock the segment when needed. Fig. 4(c) highlights the internal routing within the segment, while Fig. 3 shows the external routing. The belt attached to point A passes down to the base along each triangular segment, around a spring-loaded pulley/tensioner, back up the other side, around a pulley on point C, and attaches back to point A. The green belt is routed in a similar fashion, but is attached to point C. The kinematics of this routing are detailed in the following section, Section III-D.

According to previous literature, an empirical law for calculating resistive force F_B for one jamming layer that slides between the brake pads can be calculated as follows [44]:

$$F_B = \mu SNP \tag{1}$$

where μ is the friction coefficient between layers, S is the area of jamming, N stands for the total jammed layer number, and P represents the negative pressure on the jammed materials. A

detailed brake force evaluation can be found in the supplemental material, Section SM-4.

D. System Kinematics

We have developed two parametric models for understanding the kinematics of our locking serial mechanism. As mentioned in Section III-C, one global brake is responsible to lock all DOFs; the force required to lock is thus a function of brake dimensions and system kinematics. To understand the dimensional requirements at different configurations, a full kinematic model is required to calculate the required brake force. Two kinematic models represent the two basic segments of our system, as shown in Fig. 2: triangular, single DOF segments, and a four-bar parallel mechanism that can both translate and rotate, located at the most distal segment. Together, these two models can help us understand how belts, routed through the system, can be expected to perform when held by the brake located in the base. This can be used for a number of purposes, including verifying the performance of our current system and estimating the kinds of performance-focused redesigns required to ensure that locking forces on all joints can support similar loading conditions by the wearer. Fig. 4 highlights the details of our belt routing and system kinematic variables; our process for solving for the belt forces is summarized below.

We first specify a system configuration, defining the joint orientations and thus the location of the end-effector. The dimensions of each link, and the belt routing determines the direction of all belt tensions, which can then be solved for based on an assumption of external loading conditions. Because belts span joints with varying geometry, it is readily apparent that the effective moment arm of the belt depends on the state of the joint. A set of forces is then assigned to the end effector; these forces can be supplied either as a set of numerical or symbolic values, and can be derived from biomechanical loading assumptions based on different use-cases.

We proceed to analyze one link at a time, assuming that the selected segment is slipping, while all other joints remain fixed. This permits us to analyze the brake slip limits at each joint independently. Based on the direction of forces supplied at the end effector, only one of the two belts routed to each triangular segment will be in tension. We solve for the tensile force in each one degree-of-freedom joint required to maintain static equilibrium against external end-effector forces by formulating the problem as a constrained minimization problem, where the combination of forces must be minimized while keeping belt tensions positive.

For the final four-bar linkage, there are a total of four links and four belts, but only two total degrees of freedom, with only two belts ever in tension at a time, as shown in Fig. 5. Based on the fact that the four-bar linkage is a parallel mechanism, we can solve for the independent motion variables first, to generate the Jacobians mapping internal and external forces to each other, and then use those Jacobians to solve for the two out of four belt tensions that are holding the system in static equilibrium in that specific state. We again use a constrained minimization formulation to solve for belt tensions.

Given all the belt tensions solved for in the serial link kinematics, we then evaluate which of those tensions is the highest,

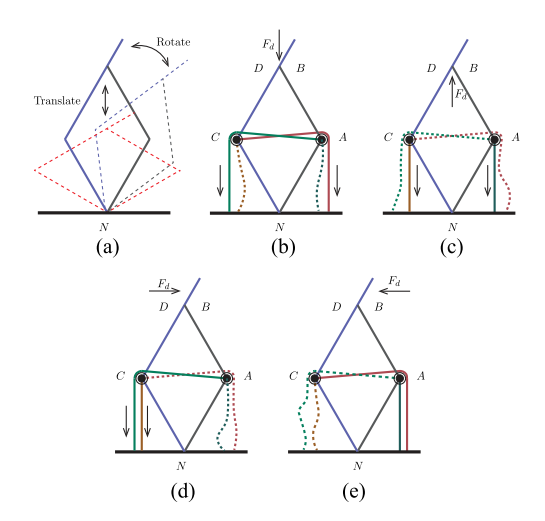


Fig. 5. Locking illustration: In (a), we show the four-bar segment exhibits both translational and rotational DOFs, as seen in the three displayed configurations. In the following set of figures, we color-code four tendons to show the activated belts under various loading conditions. Solid lines indicate the tendons in tension; the arrows denote the direction of tendon forces. The dashed lines indicate slack tendons. F_d indicates the external loading direction. (b)–(e) illustrate four Cartesian loading conditions: downward, upward, right, and left, respectively.

and what the required braking force (normal to the belts) will be, using an experimentally determined coefficient of friction. To symbolically solve the belt forces and the kinematics of each segments as well as the full-body kinematics, we model the structure in Pynamics⁵ [57], [58], a custom Python library using Kane's method to derive symbolic equations of motion. A master Python script reads the system's configuration and generates the state variables for each segments. We solve the required locking force for each triangle after calculating the four-bar locking forces using two subscripts, respectively. The corresponding scripts can be found in the repository.⁶

To understand the required forces for the segments, we first calculate the force required to lock the most distal segment under external loading, as a case study of understanding the full-body static force balances. This four-bar linkage consists of a set of *independent* joints $(q_i = [q_1, q_3])$ and *dependent* joints $(q_d = [q_2, q_4])$, as shown in Fig. 4(a) and (c), such that

$$q = \begin{bmatrix} q_i \\ q_d \end{bmatrix} = \begin{bmatrix} q_1 & q_3 & | & q_2 & q_4 \end{bmatrix}^T. \tag{2}$$

The planar four-bar linkage can be thought of as two serial RR chains connected at their respective ends via a pin joint. The motion of \vec{p}_B and \vec{p}_D , or the position of the two distal points on each serial chain are thus constrained together with the equation $\vec{z} = \vec{p}_B - \vec{p}_D = \vec{0}$. The time derivative of this vector equation with respect to the Newtonian reference frame permits us to linearize this equation with respect to the system's velocity variables \dot{q}_i and \dot{q}_d , respectively

$$\dot{\vec{z}} = \dot{\vec{p}}_B - \dot{\vec{p}}_D = \vec{0} \tag{3}$$

⁵[Online]. Available: https://github.com/idealabasu/code_pynamics

⁶[Online]. Available: https://github.com/dlisys/code_TMech_pynamics_demo

$$\dot{z} = \dot{\vec{z}} \cdot \begin{bmatrix} \hat{x} & \hat{y} \end{bmatrix}^T. \tag{4}$$

Using the relation

$$M_A = \left[\frac{\partial \dot{z}}{\partial \dot{q}_i}\right], M_B = \left[\frac{\partial \dot{z}}{\partial \dot{q}_d}\right] \tag{5}$$

we can then split z into independent and dependent parts $\dot{z} = M_A \dot{q}_i + M_B \dot{q}_d = 0$ and solve for \dot{q}_d

$$\dot{q}_d = \underbrace{\left[-M_B^{-1} M_A \right]}_C \dot{q}_i. \tag{6}$$

The Cartesian velocity of the end-effector can be expressed by the well-known equation $\dot{x} = J\dot{q}_i$, where $\dot{x} = [\vec{p}_B \cdot \hat{x} \quad \dot{\vec{p}}_D \cdot \hat{y} \quad \omega]^T$. J is derived by expressing

$$\dot{x} = J_i \dot{q}_i + J_d \dot{q}_d \tag{7}$$

where $J_i=[\frac{\partial \dot{x}}{\partial \dot{q_i}}]$ and $J_d=[\frac{\partial \dot{x}}{\partial \dot{q_d}}]$. By substituting in (6) and collecting terms

$$\dot{x} = (J_i \dot{q}_i + J_d C \dot{q}_i)
= \underbrace{(J_i + J_d C)}_{J} \dot{q}_i.$$
(8)

The flat belts used for locking the four-bar segment are routed as illustrated in Fig. 4(c), where belt l_1 is connected to point pA and then routed along the proximal triangle elements through point T_{j-1}^R , continuing to the base where it is connected to belt l_3 . Belt l_2 is attached at point pCD and routed around a virtual pulley colocated at pAB and finally routed down along right side of each triangle down to the base, connecting at the bottom to belt l_4 . On the left side, l_3 and l_4 are routed along the left side of the system in the same way, connecting to l_1 and l_2 , respectively. When clamped, however, the two sides of each belt must be considered independent, and their forces analyzed separately. The velocity \dot{l} of these four belts can be expressed as

$$\dot{l} = [\dot{l}_1 \ \dot{l}_2 \ \dot{l}_3 \ \dot{l}_4]^T = J_t \dot{q}_i \tag{9}$$

where

$$J_t = \left[\frac{\partial \dot{l}}{\partial \dot{q}_i} \right]. \tag{10}$$

We can thus equate the torques on our independent degrees of freedom q_i from the belts to the equal and opposite torque from the end-effector to the same joints. The required end-effector force $f = [f_x \ f_y \ \tau_z]^T$ can be then calculated according to the tension in the belts $f_t = [f_1 \ f_2 \ f_3 \ f_4]^T$ using the principle of virtual work to obtain

$$\tau_{ind} = J^T f = J_t^T f_t$$

$$J^T f - J_t f_t = 0. \tag{11}$$

Since the J_t is a 4 \times 2 matrix, it is clear that the four forces from the brakes act redundantly on the system. Because, however, they can only act in tension, a valid solution for obtaining static equilibrium must ignore cases when tension in the belts is negative. To solve this problem we formulate it as a constrained minimization problem, minimizing the sum of the square of the belt tensions at a given external tip force, while in a specific

configuration as

$$min - f_{t(i)}^T f_{t(i)}$$
 (12)

subject to

$$g(f_t): J^T f - J_t f_t = 0 (13)$$

$$h(f_t): f_t \ge 0. (14)$$

We calculate $f_{min}(q)$ at different configurations of the fourbar as a function of q. The resulting minimum force solution can be then used to determine the locking force requirements for the four bar on the top.

We also model the force interactions of the *i*th triangular segment at an arbitrary location as shown in Fig. 4(b). The distal hinge of this triangle is connected to the base of the distal four-bar segment. The belts on the triangle are connected to the corresponding vertices of the successive triangle and shown in Fig. 4(b) as l_5 , l_6 . As the triangles are connected to the successive element on its top vertices and the motion of four-bar element will not affect the triangles, we simplify the kinematics to serial linkages.

For example, to solve for equilibrium in the kth triangle, we create a virtual link L_a connected to the bottom of this triangle, rotated around the origin. The remainder of this system can be then simplified to a virtual link L_b rotated along the first link. The length and angular velocities (L_a, L_b, q_a) of the system can then be calculated according to the configuration of the device.

The Cartesian velocity of the end-effector $(\dot{x} = \dot{\vec{p}}_B \cdot [\hat{x} \quad \hat{y}]^T)$ can be expressed as

$$\dot{x} = J\dot{q}_i \tag{15}$$

where $J=[\frac{\partial \dot{x}}{\partial \dot{q_i}}]$. The velocities $\dot{l_t}$ of the layers mounted on the triangles can be expressed as

$$\dot{l_t} = \left[\dot{l_5}, \dot{l_6}\right]^T = J_i q_i \tag{16}$$

$$J_t = \left\lceil \frac{\partial \dot{l}_t}{\partial \dot{q}_i} \right\rceil. \tag{17}$$

The triangle belt velocities can be then related to the independent end-effector velocities. The minimal layer forces $f_t = [f_5, f_6]^T$ under external load, f can be calculated using a similar approach described in (11) to (14) and formulated as

$$min - (f_5^2 + f_6^2)$$
 (18)

subject to

$$g(f_t): J^T f - J_t f_t = 0 (19)$$

$$h(f_t): f_t \ge 0. (20)$$

We obtain the minimal layer force for the triangles. By modifying the orientation of the triangle and the corresponding belts, we then are able to solve each triangles at an arbitrary location.

IV. RESULTS AND ANALYSIS

A. Kinematic Model Verification

We perform a series of tests measuring the external load required to deform the linkage while changing the configuration and locking forces to verify the static force model presented in

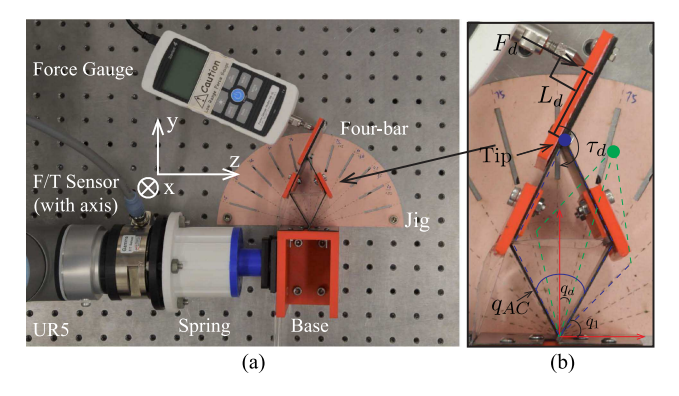


Fig. 6. Four-bar element locking test. In (a), we show the overview of the experiments and label each piece of equipment. The spring is mounted within the white case between the F/T sensor and the base. The alignment jig (in pink) is installed under the four-bar segment. We highlight how forces are applied to the distal link in (b) and label how we define the joint angles, inner angle and orientation, consistent with q_1 , q_{AC} , and q_a in Fig. 4.

Section III-D. We use a UR5 robot arm with a spring and a load cell attached at its end effector to adjust the locking pressure, as shown in Fig. 6(a). According to Hooke's law, compressing the spring installed inside the white case between the brake pad and the base station increases the locking force. We record the z-axis force of the load cell and control the robot's displacement simultaneously using a python script. The robot arm stops once the force threshold is reached in order to maintain constant clamping pressure.

In this set of tests, the length of each link in this four-bar is 30 mm. After adjusting the four-bar mechanism's joint angles and orientation, we lock the four-bar using the test setup by compressing the locking pad to constrain the motion of the belts. For the purposes of validating the kinematics and to ensure that the stiffness of the flexure joints do not add noticeable stiffness to the system, we have selected a thinner flexible material for the hinge layer of the laminated origami structure. To measure the external loads applied to the tip, we use a Mark-10 M4-10 force gauge to push distal link of the four bar normal to the surface until the layer slips at each configuration, where the distance to the tip of the four-bar, L_d is 30 mm. During the test, we record the maximum force required to initiate slip in the belts and then from that value calculate the equivalent holding torque. In each combination of joint angle and orientation, we repeat the test ten times to obtain the average external torque to deform the mechanism, $\bar{T_d}^f$ as $\bar{T_d}^f = \bar{F_d}^f L_d$. We have tested the device under a series of sym-

We have tested the device under a series of symmetric configurations about the four joint angles, $q_1 = [30^\circ, 45^\circ, 60^\circ, 75^\circ]^T$ and four values for the inner joint angle $q_{AC} = [30^\circ, 60^\circ, 90^\circ, 120^\circ]^T$, as shown in Fig. 7(a). We use a laser-cut alignment jig to align the links according to each configuration. As the tip torque is manually measured and applied, using smaller clamping forces improves the accuracy of our results by reducing the deformation that would be present in the system under higher loads. We thus apply 2 N of force along the force/torque sensor's z-axis to clamp the belts in this experiment. We then changed the orientation q_a of the segment to create

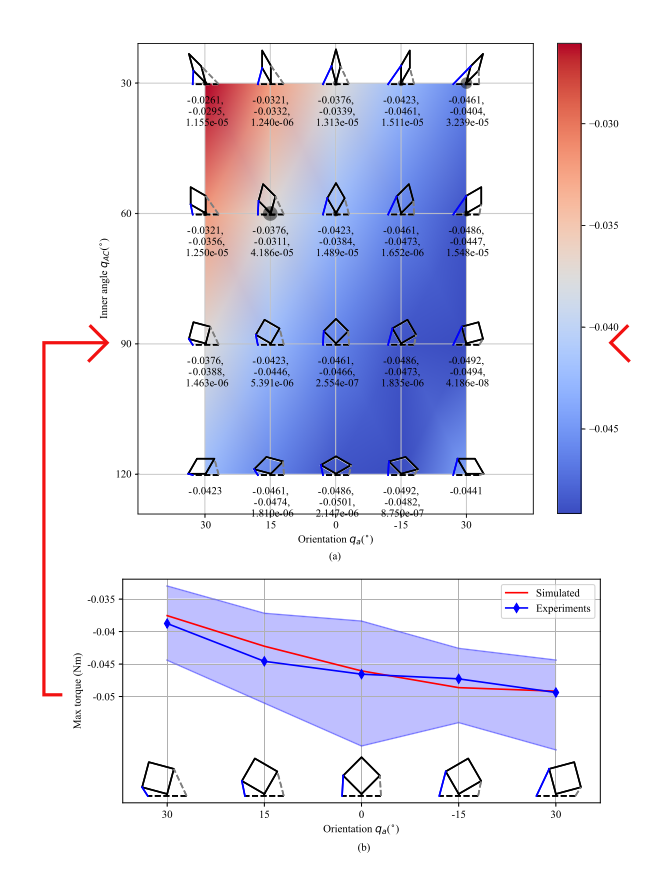


Fig. 7. Kinematic model validation. In (a), we show the maximum simulated holding torque of the four-bar using the continuous contour plot. Experimental values, located at each grid element under the black dots show the simulated torque, measured average torque from experiments, and RMSE between these two values, respectively. The size of the black dot indicates the RMSE. We plot the current configuration of the four bar with base and belt at each combination of orientation and inner joint angle. As the experiments for $(30^\circ, 120^\circ)$ and $(-30^\circ, 120^\circ)$ are not performed, we show the configuration and simulated value only. In (b), we show how the four-bar holding torque changes according to the orientation of the linkage. The blue solid line indicates the experimental values and the blue region beneath it shows the range of experimental values measured from the tests, while the red solid line shows the model estimate.

asymmetric scenarios and validate our kinematics across a larger workspace. In this set of experiments, the orientation, q_a was set to $[-30^\circ, -15^\circ, 0^\circ, 15^\circ, 30^\circ]^T$ of the inner angle we measured before. When the inner angle is 120° and the orientation is set to -30° or 30° , the lower link of the four bar mechanism interferes with the base. We thus skip this two sets of experiments. A total of 18 (4 \times 5-2) of subtests were thus performed in Fig. 7.

The average measured friction force f_r measured using the test setup is 1.56 N. We then use the following Jacobian matrix, J_t in its numerical form obtained from the Pynamics code generated using the method described in Section III-D to relate the belt forces, $[f_1, f_2, f_3, f_4]^T$ to the independent torque, $[T_1, T_2]^T$ of the four-bar.

$$\underbrace{\begin{bmatrix} c_1 \ c_2 \ c_3 \ c_4 \\ c_5 \ c_6 \ c_7 \ c_8 \end{bmatrix}}_{J_t} \begin{bmatrix} f_1 \\ f_2 \\ f_3 \\ f_4 \end{bmatrix} = \begin{bmatrix} T_1 \\ T_2 \end{bmatrix}.$$
(21)

imen the better the form of the control of the con

⁷0.002 mil Dura-Lar Plastic Film

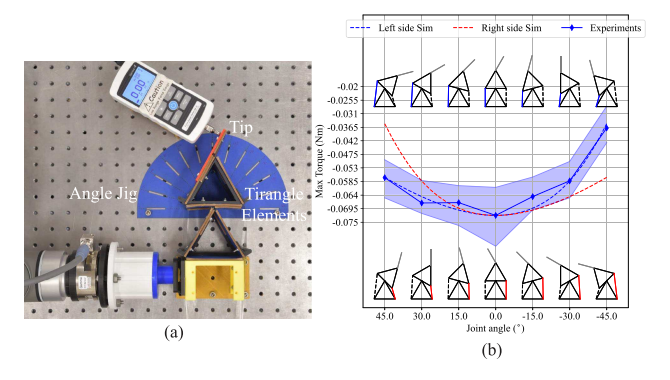


Fig. 8. In this figure, we present the test setup for validating triangle element kinematics and show the result. In (a), we replace the four-bar linkage with the triangle segments, base and the angle measurement. The test is performed in a similar manner as described for validating the four bar. In (b), we compare the estimate for the maximum torque the triangle can hold across different configurations against the experimental data, where the solid line is the mean experimental value, the dashed lines indicate the model estimate, and blue region shows the range of experimental values collected at each point.

During the test, the external torque is applied to link p_{DB}^{-} and the left side link, the right side of the four-bar and the belts are thus in a slack state, meaning no belt force is applied. We thus simplify (21) to

$$\begin{bmatrix} c_2 c_3 \\ c_6 c_7 \end{bmatrix} \begin{bmatrix} f_2 \\ f_3 \end{bmatrix} = \begin{bmatrix} T_1 \\ T_2 \end{bmatrix}. \tag{22}$$

The tip torque τ_{tip} can be calculated as $\tau_{tip} = T_1 + T_2$. We use the following optimization routine to calculate the maximum external torque the four-bar linkage can hold:

min:
$$-(T_1 + T_2)^2$$

 $-(c_2f_2 + c_3f_3 + c_5f_2 + c_6f_3)^2$ (23)

subject to

$$h(f_2, f_3) : \begin{bmatrix} 0 \\ 0 \end{bmatrix} \le \begin{bmatrix} f_2 \\ f_3 \end{bmatrix} \le \begin{bmatrix} f_r \\ f_r \end{bmatrix}. \tag{24}$$

We then obtain the maximum holding torque the four-bar is able to provide and compare with the \overline{T}_d values experimentally measured, as shown in Fig. 7(a).

Although these mechanisms are implemented in the full prototype, some configurations including the belt routing and base location are different. We thus developed two separate simulations to mirror the experimental setups. These may be found in the code repository, where a detailed description of the approach can be found.

Using a similar approach, we also validated the kinematics of the triangle element, where the length of the sides is 85 mm. We use the same test setup previously introduced in this section, but replace the base to fit the new triangular element, as seen in Fig. 8(a). We use the force gauge to push the tip of the upper triangle element, T_2 across joint angle, $q_b = [-30^{\circ}, -15^{\circ}, 0^{\circ}, 15^{\circ}, 30^{\circ}]$ and average the reading to obtain the torque required to deform the triangle as \bar{T}_d^t seen in Fig. 8(b).

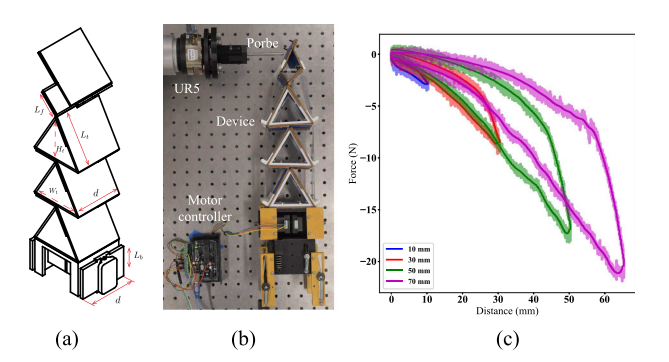


Fig. 9. System dimension and loading capability experiments. In (a), we show a sketch of the robot with labeled dimensions. (b) illustrates the test setup. In (c), we show the filtered load cell force versus distance using the solid lines. The light colored lines indicate the unfiltered raw data. We notice the deviation between 40 mm data' slope and we attribute this to the complex kinematics and initial states of the device.

TABLE II
ROBOT PARAMETER

Parameter	Value	Description
L_f	40 mm	Four-bar length
L_t	85 mm	Triangle length
H_t	73 mm	Triangle height
W_t	85 mm	Triangle width
L_b	75 mm	Brake length
d	80 mm	Depth

In Fig. 8(b), the blue line indicates the condition where the left belt is locked and an external torque is applied clockwise, illustrated along the top of Fig. 8(b). The blue transparent area indicates experimental error between runs, while the blue solid line indicates the mean of experimental data; the dashed blue line represents model results. As pushing along the right side yields a mirrored result, we mirror the model results, presented as a red dashed line.

As mentioned in Fig. 4(b), the belt routed between links forms a triangle; this means that the moment arm of each belt is a function of the each joint's configuration. This influences the locking forces available at each joint, requiring us to calculate the braking force required as a function of system configuration. To help dimension of the device, we must analyze the *worst-case* scenario.

B. Dimension Selection and Full System Kinematics

We select the following dimensions for the mechanism, as illustrated in Fig. 9 and listed in Table II. We use two NEMA 17 stepper motors ($42 \text{ mm} \times 42 \text{ mm} \times 34 \text{ mm}$) inside the base; the width of both the triangle and base are 85 mm. In the current design, we use three equilateral triangles (73 mm height) and one four-bar linkage with a joint length of 40 mm on the top. Using the kinematic models developed in Section III-D and the torque requirements from the human study [59], we have determined the braking forces required for locking the robot are at least 60 N when the device is straight. Using (1), with a static friction coefficient of 0.017 (measured in Section SM-4), we calculate that the minimum required area for the brake pad is 5200 mm^2 . Considering the screw hole in the middle of the brake pad

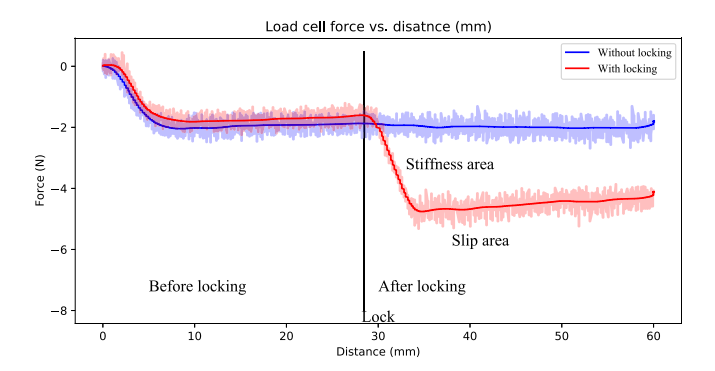


Fig. 10. System-level locking test. We compare the load cell force with and without locking (0.5 A current) using red and blue solid lines correspondingly, where the transparent error bar indicates the raw data. We activate the brake at around 28 mm, where we draw a black vertical line to indicate the locking.

(r = 5.25 mm), the length of the brake (L_b) is set as $5200/(80 - 5.25 \times 2) = 74.8$; we thus use a 75 mm long brake pad.

The kinematic analysis also confirms that the four-bar linkage is the weakest joint in this system. We attribute that to the fact that the total effective width of the belts connected to the four-bar segment is half of those connected to the triangular segments, in order to accommodate the routing of four separate belts into the 2-DOF segment.

To test the system-level stiffness, we fully assemble the spine device, mount the device to the test bed horizontally, and attach the brake system as shown in Fig. 9(a). During the test, a Python script locks the belts when the device is straight and commands the UR5 to push the end-effector with a metal probe. The robot arm then returns to its original position after it pushes the probe forward a set distance. We then compare the z-axis direction load cell force for four distances, 10, 30, 50, and 70 mm to understand the stiffness of the system. We then start to push the robot in locking state using the force gauge to understand the slippage limit using a similar setup in Fig. 6. We repeat the test for ten times and the average force required to deform the robot is 56.5 N. We attribute this deviation to the design goal (60 N) to the assembling and misalignment error of the system. In these test we found that the first joint to slip was the four-bar, confirming the kinematic model's braking force estimates.

C. System-Level Lock and Unlock

In this section, we use the same test setup in Fig. 9(a) and start pushing the device in the unlocked state using low motor current to measure the locking speed of the robot to prevent damage to the load cell. As the robot is a passive device that can be stiffened on demand, locking speed became the most important—and only—metric for system response. After the tip of the UR5 passes the straight, vertical configuration of the device, the device is locked as the UR5 continues moving. We use the force from the load cell to differentiate between locked and unlocked states. Before the test starts, the probe does not contact the device for calibration purposes; when the probe begins to contact the spine mechanism, a small -z direction force can be seen (starting around t = 5 s)—due to system joint stiffness and belt friction—in Fig. 10. The load cell force increases after the lock activates (as shown in the red solid line).

We compare the load cell reading against the unlocked system (in blue) and estimate that the brake's locking time is around 0.1 s, which is a sufficient response time for supporting the trunk, according to preliminary human subject studies.

V. CONCLUSION AND FUTURE WORK

We have presented a origami-inspired mechanism with embedded sensing capabilities as well as extensibility for connecting external sensors. We mechanically clamp the sliding layers to design a laminar jamming inspired brake. We estimate the joint angle and end pose using the integrated sensor and reveal its potential in wearable robotics.

We believe that origami inspired "exo-shell" structures can bridge the gap between rigid exoskeletons and soft exo-suits in a way that balances the compromises of both. Introducing origami-inspired techniques into wearable robotics permits us to provide light weight, low cost, and rapidly manufacturable solutions for each user. Our selected manufacturing technique facilitates rapid iteration of designs while producing highly capable wearable prototypes. Currently, this device is designed on to be mounted on the human back to provide external support. By modifying the arrangement and dimension of structural elements, brakes, and supporting components, this development strategy can be easily adapted for wearable applications about other parts of the human body.

Future work includes optimizing the overall dimensions based on a biomechanics study planned with our collaborators on healthy elderly human subjects. Our aim will be to evaluate the hypothesis that timed stiffening of the system can improve the stability and reduce torques about the trunk during obstacle avoidance. Currently, this device is mounted at the spine of the subject. However, we find that the kinematics of larger arrays of this specific tessellated pattern exhibits highly constrained motion, making it less compatible with the types of motion experienced around the human torso. We aim to address this by investigating more complex, stiffenable, 2-D origami patterns such as the waterbomb and herringbone patterns. Another improvement will be to modularize the braking system to eliminate the base-mounted spring tensioner and reduce the system-level design complexity. To reduce the number of sensors and estimate the full body pose with more affordable embedded sensing techniques, sensor fusion algorithms are also currently being developed.

ACKNOWLEDGMENT

TGKC is a research alliance between Arizona State University and The KAITEKI Institute, an affiliate of the Mitsubishi Chemical Group. The authors would like to thank Dr. Aukes' lab member, Fuchen Chen for providing the laminate-pipeline python script.

REFERENCES

- J. C. Perry, J. Rosen, and S. Burns, "Upper-limb powered exoskeleton design," *IEEE/ASME Trans. Mechatronics*, vol. 12, no. 4, pp. 408–417, Aug. 2007.
- [2] H. Kazerooni, J.-L. Racine, L. Huang, and R. Steger, "On the Control of the Berkeley Lower Extremity Exoskeleton (bleex)," in *Proc. IEEE Int. Conf. Robot. Autom.*, 2005, pp. 4353–4360.

- [3] A. Zoss, H. Kazerooni, and A. Chu, "Biomechanical design of the Berkeley lower extremity exoskeleton (bleex)," *IEEE/ASME Trans. Mechatronics*, vol. 11, no. 2, pp. 128–138, Apr. 2006.
- [4] J. Pratt, B. Krupp, C. Morse, and S. Collins, "The roboknee: An exoskeleton for enhancing strength and endurance during walking," in *Proc. IEEE Int. Conf. Robot. Autom.*, 2004, vol. 3, pp. 2430–2435.
- [5] A. Chu, H. Kazerooni, and A. Zoss, "On the biomimetic design of the berkeley lower extremity exoskeleton (bleex)," in *Proc. IEEE Int. Conf. Robot. Autom.*, 2005, pp. 4345–4352.
- [6] C. J. Walsh, K. Endo, and H. M. Herr, "A quasi-passive leg exoskeleton for load-carrying augmentation," *Int. J. Humanoid Robot.*, vol. 4, no. 03, pp. 487–506, 2007.
- [7] F. H. M. van Herpen, R. B. van Dijsseldonk, H. Rijken, N. L. W. Keijsers, J. W. K. Louwerens, and I. J. W. van Nes, "Case report: Description of two fractures during the use of a powered exoskeleton," *Spinal Cord Ser Cases*, vol. 5, no. 1, pp. 1–4, Dec. 2019.
- [8] A. F. Pérez Vidal et al., "Soft exoskeletons: Development, requirements, and challenges of the last decade," *Actuators*, vol. 10, no. 7, p. 166, Jul. 2021, doi: 10.3390/act10070166.
- [9] Y. Ding et al., "Biomechanical and physiological evaluation of multi-joint assistance with soft exosuits," *IEEE Trans. Neural Syst. Rehabil. Eng.*, vol. 25, no. 2, pp. 119–130, Feb. 2017.
- [10] Y. Mengüç et al., "Wearable soft sensing suit for human gait measurement," Int. J. Adv. Robot. Syst., vol. 33, no. 14, pp. 1748–1764, Dec. 2014.
- [11] L. N. Awad et al., "A soft robotic exosuit improves walking in patients after stroke," Sci. Transl. Med., vol. 9, no. 400, Jul. 2017, Art. no. eaai9084.
- [12] B. T. Quinlivan et al., "Assistance magnitude versus metabolic cost reductions for a tethered multiarticular soft exosuit," *Sci. Robot.*, vol. 2, no. 2, Jan. 2017, Art. no. eaah4416.
- [13] T. Kermavnar, K. J. O'Sullivan, A. de Eyto, and L. W. O'Sullivan, "Discomfort/Pain and tissue oxygenation at the lower limb during circumferential compression: Application to soft exoskeleton design," *Hum Factors*, vol. 62, no. 3, pp. 475–488, May 2020.
- [14] B. T. Quinlivan et al., "Assistance magnitude versus metabolic cost reductions for a tethered multiarticular soft exosuit," *Sci. Robot.*, vol. 2, no. 2, Jan. 2017, Art. no. eaah4416.
- [15] S. Lee et al., "Autonomous multi-joint soft exosuit with augmentation-power-based control parameter tuning reduces energy cost of loaded walking," *J. NeuroEng. Rehabil.*, vol. 15, no. 1, pp. 1–9, Dec. 2018.
- [16] B. S. Rupal, S. Rafique, A. Singla, E. Singla, M. Isaksson, and G. S. Virk, "Lower-limb exoskeletons: Research trends and regulatory guidelines in medical and non-medical applications," *Int. J. Adv. Robot. Syst.*, vol. 14, no. 6, pp. 1–27, Nov. 2017.
- [17] "PhoeniX suitx," 2022. [Online]. Available: https://vandrico.com/ wearables/device/suitx-phoenix.html
- [18] A. Collo, V. Bonnet, and G. Venture, "A quasi-passive lower limb exoskeleton for partial body weight support," in *Proc. 6th IEEE BioRob*, 2016, pp. 643–648.
- [19] A. Salmoiraghi and D. Akin, "Review of wearable robotic assistive devices for integration with pressure suit arms," in *Proc. 42nd Int. Conf. Environ.* Syst., 2012, Art. no. 3487.
- [20] K. N. Gregorczyk, L. Hasselquist, J. M. Schiffman, C. K. Bensel, J. P. Obusek, and D. J. Gutekunst, "Effects of a lower-body exoskeleton device on metabolic cost and gait biomechanics during load carriage," *Ergonomics*, vol. 53, no. 10, pp. 1263–1275, 2010.
- [21] N. A. Taylor, G. E. Peoples, and S. R. Petersen, "Load carriage, human performance, and employment standards," *Appl. Physiol., Nutr., Metab.*, vol. 41, no. 6 (Suppl. 2), pp. S131–S147, 2016.
- [22] A. Grabowski, C. T. Farley, and R. Kram, "Independent metabolic costs of supporting body weight and accelerating body mass during walking," *J. Appl. Physiol.*, vol. 98, no. 2, pp. 579–583, Feb. 2005.
- [23] L. Cao, A. T. Dolovich, A. L. Schwab, J. L. Herder, and W. C. Zhang, "Toward a unified design approach for both compliant mechanisms and rigid-body mechanisms: Module optimization," *J. Mech. Des.*, vol. 137, no. 12, 2015, Art. no. 122301.
- [24] A. Chen, R. Yin, L. Cao, C. Yuan, H. Ding, and W. Zhang, "Soft robotics: Definition and research issues," in *Proc. 24th Int. Conf. Mechatronics Mach. Vis. Pract.*, 2017, pp. 366–370.
- [25] E. W. Hawkes et al., "Programmable matter by folding," *Proc. Nat. Acad. Sci.*, vol. 107, no. 28, pp. 12441–12445, 2010.
- [26] S. M. Felton, M. T. Tolley, E. D. Demaine, D. Rus, and R. J. Wood, "A method for building self-folding machines," *Science*, vol. 345, no. 6197, pp. 644–646, 2014.

- [27] E. T. Filipov, T. Tachi, and G. H. Paulino, "Origami tubes assembled into stiff, yet reconfigurable structures and metamaterials," *Proc. Nat. Acad.* Sci., vol. 112, no. 40, pp. 12321–12326, 2015.
- [28] S. Mintchev, J. Shintake, and D. Floreano, "Bioinspired dual-stiffness origami," *Sci. Robot.*, vol. 3, no. 20, 2018, Art. no. eaau0275.
- [29] Z. Zhai, Y. Wang, and H. Jiang, "Origami-inspired, on-demand deployable and collapsible mechanical metamaterials with tunable stiffness," *Proc. Nat. Acad. Sci.*, vol. 115, no. 9, pp. 2032–2037, 2018.
- [30] A. Firouzeh and J. Paik, "Robogami: A fully integrated low-profile robotic origami," *Asme Jmr*, vol. 7, no. 2, 2015, Art. no. 021009.
- [31] C. H. Belke and J. Paik, "Mori: A modular origami robot," *IEEE-ASME Trans. Mechatronics*, vol. 22, no. 5, pp. 2153–2164, Oct. 2017.
- [32] A. Firouzeh and J. Paik, "An under-actuated origami gripper with adjustable stiffness joints for multiple grasp modes," Smart Mater. Struct., vol. 26, no. 5, Apr. 2017, Art. no. 055035.
- [33] K. Liu, T. Tachi, and G. H. Paulino, "Invariant and smooth limit of discrete geometry folded from bistable origami leading to multistable metasurfaces," *Nature Commun.*, vol. 10, no. 1, pp. 1–10, 2019.
- [34] B. H. Hanna, J. M. Lund, R. J. Lang, S. P. Magleby, and L. L. Howell, "Waterbomb base: A symmetric single-vertex bistable origami mechanism," *Smart Mater. Struct.*, vol. 23, no. 9, 2014, Art. no. 094009.
- [35] B. Sargent et al., "An origami-based medical support system to mitigate flexible shaft buckling," ASME. J. Mechanisms Robot., vol. 12, no. 4, Aug. 2020, Art. no. 04100.
- [36] D. M. Aukes et al., "Design and testing of a selectively compliant underactuated hand," *Int. J. Robot. Res.*, vol. 33, no. 5, pp. 721–735, 2014.
- [37] H. Banerjee, T. K. Li, G. Ponraj, S. K. Kirthika, C. M. Lim, and H. Ren, "Origami-Layer-Jamming deployable surgical retractor with variable stiffness and tactile sensing," *J. Mechanisms Robot.*, vol. 12, no. 3, 2020, Art. no. 031010.
- [38] A. R. Deshpande, Z. T. H. Tse, and H. Ren, "Origami-inspired bidirectional soft pneumatic actuator with integrated variable stiffness mechanism," in *Proc. 18th Int. Conf. Adv. Robot.*, 2017, pp. 417–421.
- [39] B. Aktaş, Y. S. Narang, N. Vasios, K. Bertoldi, and R. D. Howe, "A modeling framework for jamming structures," *Adv. Funct. Mater.*, vol. 31, no. 16, 2021, Art. no. 2007554.
- [40] Y. S. Narang, J. J. Vlassak, and R. D. Howe, "Mechanically versatile soft machines through laminar jamming," *Adv. Funct. Mater.*, vol. 28, no. 17, 2018, Art. no. 1707136.
- [41] C. S. Lee, S. GodageIsuru GonthinaPhanideep, and D. WalkerIan, "Soft robots and Kangaroo tails: Modulating compliance in continuum structures through mechanical layer jamming," *Soft. Robot.*, vol. 3, no. 2, pp. 54–63, 2016.
- [42] Y. Lin et al., "Controllable stiffness origami "skeletons" for lightweight and multifunctional artificial muscles," Adv. Funct. Mater., vol. 30, no. 31, 2020. Art. no. 2000349.
- [43] D. Shah, E. J. Yang, M. C. Yuen, E. C. Huang, and R. Kramer-Bottiglio, "Jamming skins that control system rigidity from the surface," *Adv. Funct. Mater.*, vol. 31, no. 1, 2020, Art. no. 2006915.
- [44] Y. Kim, S. Cheng, S. Kim, and K. Iagnemma, "A novel layer jamming mechanism with tunable stiffness capability for minimally invasive surgery," *IEEE Trans. Robot.*, vol. 29, no. 4, pp. 1031–1042, Aug. 2013.
- [45] Y. Jiang, D. Chen, C. Liu, and J. Li, "Chain-like granular jamming: A novel stiffness-programmable mechanism for soft robotics," *Soft Robot.*, vol. 6, no. 1, pp. 118–132, Feb. 2019.
- [46] P. M. Loschak, S. F. Burke, E. Zumbro, A. R. Forelli, and R. D. Howe, "A robotic system for actively stiffening flexible manipulators," in *Proc. IEEE/RSJ Int. Conf. Intell. Robots Syst.*, 2015, pp. 216–221.
- [47] X. Yang et al., "Spine-inspired continuum soft exoskeleton for stoop lifting assistance," *IEEE Robot. Autom. Lett.*, vol. 4, no. 4, pp. 4547–4554, Oct. 2019.
- [48] D. Lee, S. Kim, H.-J. Park, S. Kim, and D. Shin, "A spine assistive robot with a routed twisted string actuator and a flat-back alleviation mechanism for lumbar-degenerative flat back," *IEEE/ASME Trans. Mechatron.*, to be published, doi: 10.1109/TMECH.2022.3175298.
- [49] U. Heo, S. J. Kim, and J. Kim, "Backdrivable and fully-portable pneumatic back support exoskeleton for lifting assistance," *IEEE Robot. Autom. Lett.*, vol. 5, no. 2, pp. 2047–2053, Apr. 2020.
- [50] J.-H. Park, P. R. Stegall, D. P. Roye, and S. K. Agrawal, "Robotic spine exoskeleton (RoSE): Characterizing the 3-D stiffness of the human torso in the treatment of spine deformity," *IEEE Trans. Neural Syst. Rehabil. Eng.*, vol. 26, no. 5, pp. 1026–1035, May 2018.
- [51] T. S. Masood Nevisipour and H. Lee, "Trunk control in young healthy adults requires large adaptations during and after obstacle avoidance with a cognitive task," in *Proc. 45th Annu. Meeting Amer. Soc. Biomech.*, 2021, p. 420.

- [52] D. Boffey, I. Harat, Y. Gepner, C. L. Frosti, S. Funk, and J. R. Hoffman, "The physiology and biomechanics of load carriage performance," *Mil. Med.*, vol. 184, no. 1-2, pp. e83–e90, Jan. 2019.
- [53] J. N. Caldwell, L. Engelen, C. van der Henst, M. J. Patterson, and N. A. S. Taylor, "The interaction of body armor, low-intensity exercise, and hot-humid conditions on physiological strain and cognitive function," *Mil. Med.*, vol. 176, no. 5, pp. 488–493, May 2011.
- [54] D. M. Aukes, B. Goldberg, M. R. Cutkosky, and R. J. Wood, "An analytic framework for developing inherently-manufacturable pop-up laminate devices," *Smart Mater. Struct.*, vol. 23, no. 9, Aug. 2014, Art. no. 094013.
- [55] D. M. Aukes and R. J. Wood, "Popupcad: A tool for automated design, fabrication, and analysis of laminate devices," in *Proc. Micro- Nanotechnol. Sensors*, Syst., Appl. VII. Spie, 2015, pp. 169–178.
- [56] M. T. Tolley, S. M. Felton, S. Miyashita, D. Aukes, D. Rus, and R. J. Wood, "Self-folding origami: Shape memory composites activated by uniform heating," *Smart Mater. Struct.*, vol. 23, no. 9, Sep. 2014, Art. no. 094006.
- [57] M. Sharifzadeh, Y. Jiang, and D. M. Aukes, "Reconfigurable curved beams for selectable swimming gaits in an underwater robot," *IEEE Robot. Autom. Lett.*, vol. 6, no. 2, pp. 3437–3444, Apr. 2021.
- [58] D. Li, S. Huang, Y. Tang, H. Marvi, J. Tao, and D. Aukes, "Compliant fins for locomotion in granular media," *IEEE Robot. Autom. Lett.*, vol. 6, no. 3, pp. 5984–5991, Jul. 2021.
- [59] T. S. Masood Nevisipour and H. Lee, "In preparation-multi-tasking deteriorates trunk movement control during and after obstacle avoidance," *Hum. Movement Sci.*, 2022.



Dongting Li (Graduate Student Member, IEEE) received the B.S. degree in mechanical engineering from Shandong University, Shandong, China, in 2018. He is currently working toward the Ph.D. degree in systems engineering with Arizona State University, Mesa, AZ, USA.

His research interest includes the origamiinspired and laminate designs.



Emiliano Quinones Yumbla (Graduate Student Member, IEEE) received the B.S. degree in mechanical engineering from University of Puerto Rico, San Juan, Puerto Rico, in 2017. He is currently working toward the Ph.D. degree in mechanical engineering at Arizona State University, Tempe, AZ, USA.

His research interests include wearable soft robots.



Alyssa Olivas received the B.S. degree in biological sciences and the Ph.D. degree in biomedical engineering from the University of Texas at El Paso (UTEP), El Paso, TX, USA, in 2017 and 2022, respectively.

She is currently a Postdoctoral Research Scholar at Arizona State University. Her research interests include clinical biomechanics and gait analysis. Her dissertation focused on lower extremity biomechanics in children with Autism Spectrum Disorder.



Thomas Sugar (Senior Member, IEEE) received the B.S.E. degree in mechanical engineering from the University of Pennsylvania, Philadelphia, PA, USA, in 1991, the second B.S.E. degree in entrepreneurial management from The Wharton School of Business, University of Pennsylvania in 1991, and the M.S.E. and Ph.D. degrees in mechanical engineering from the University of Pennsylvania, Philadelphia, PA, USA, in 1992 and 1999, respectively.

He is a Professor and the graduate program chair for engineering and manufacturing engineering with the School of Manufacturing Systems and Networks. Arizona State University Lle

of Manufacturing Systems and Networks, Arizona State University. He works in the areas of wearable robotics to improve worker wellness and improve the quality of life.

Dr. Sugar is an ASME Fellow.



Heni Ben Amor received the Ph.D. degree in computer science from the Technical University Freiberg, Freiberg, Germany, in 2010, focusing on artificial intelligence and machine learning.

He is an Associate Professor, was previously a Research Scientist at Georgia Tech's Institute for Robotics and Intelligent Machines, where he led a project to improve robots for future applications in industrial settings, especially manufacturing. Prior to moving to Georgia Tech, he

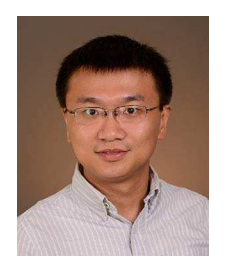
worked with Jan Peters at the Technical University Darmstadt as a Postdoctoral Scholar. His research topics focus on artificial intelligence, machine learning, human–robot interaction, robot vision, and automatic motor skill acquisition.



Hyunglae Lee (Member, IEEE) received the B.S. and M.S. degrees in mechanical and aerospace engineering from Seoul National University, Seoul, South Korea, in 2022 and 2004, respectively, and the Ph.D. degree in mechanical engineering from the Massachusetts Institute of Technology, Cambridge, MA, USA, in 2013.

He is an Associate Professor of mechanical and aerospace engineering with the Arizona State University (ASU). He currently directs the

Neuromuscular Control and Human Robotics Laboratory. Prior to joining ASU, he worked as a Postdoctoral Fellow with Sensory Motor Performance Program, Shirley Ryan AbilityLab, and also worked at Korea Institute of Science and Technology and LG Electronics. His research interest lies at the intersection of robotics, biomechanics and neuromuscular control.



Wenlong Zhang (Member, IEEE) received the B.Eng. degree (Hons.) in control science and engineering from Harbin Institute of Technology, Harbin, China, and the M.S. degree in mechanical engineering, the M.A. degree in statistics, and Ph.D. degree in mechanical engineering, all from the University of California, Berkeley, CA, USA, in 2010, 2012, 2013, and 2015, respectively.

He is currently an Associate Professor with the Polytechnic School at ASU, where he di-

rects the RISE Laboratory. His research interests include dynamic systems and control, wearable and flexible robotics, and human-machine collaboration.



Daniel M. Aukes (Member, IEEE) received the B.S. degree in mechanical engineering from Northwestern University, Evanston, IL, USA, in 2004 and the M.S. and Ph.D. degrees in mechanical engineering from Stanford University, Stanford, CA, USA, in 2009 and 2013, respectively.

He is currently an Assistant Professor with the Ira A. Fulton Schools of Engineering, Arizona State University, Mesa, AZ, USA. His Postdoctoral work with Harvard University focused on

the design and manufacturing of laminate robots. His current research interests include design and manufacture of affordable mobile robots using dynamics and simulation.